Visual Abstract

Compressive behavior of Co-Cr-Mo radially graded porous structures under as-built and heat-treated conditions

Francesco Cantaboni, Paola S. Ginestra, Marialaura Tocci, Andrea Avanzini, Elisabetta Ceretti, Annalisa Pola

Department of Mechanical and Industrial Engineering, University of Brescia, Via Branze 38, 25123 Brescia, Italy
f.cantaboni@unibs.it, https://orcid.org/0000-0003-4208-2430
paola.ginestra.cantaboni@unibs.it, https://orcid.org/0000-0002-3858-7789
marialaura.tocci@unibs.it, https://orcid.org/0000-0002-7515-0615
andrea.avanzini@unibs.it, https://orcid.org/0000-0002-7188-7687
elisabetta.ceretti@unibs.it, https://orcid.org/0000-0002-0091-8415
annalisa.pola@unibs.it, https://orcid.org/0000-0002-0722-6518

ABSTRACT. Additive manufacturing research is continuously growing, and this field requires a full improvement of the capability and reliability of the processes involved. Of particular interest is the study of complex geometries production, such as lattice structures, which may have a potentially huge field of application, especially for biomedical products.
In this work, the powder bed fusion technique was utilized to manufacture lattice structures with defined building angles concerning the build platform. A biocompatible Co-Cr-Mo alloy was used. Three different types of elementary cell geometry were selected: Face Centered Cubic, Diagonal, and Diamond. These cells were applied to the radially oriented lattice structures to evaluate the influence of their orientation in relation to the sample and the build platform. Moreover, heat treatment was carried out to study its influence on microstructural properties and mechanical behavior. Microhardness was measured, and compressive tests were performed to detect load response and to analyse the fracture mechanisms of these structures.
The results show that the mechanical properties are highly influenced by the cell orientation in relation to the building direction and that the properties can be further tuned via HT. The favorable combination of mechanical properties and biocompatibility suggests that Co-Cr-Mo lattices may represent an optimal solution to produce customized metal implants.

KEYWORDS. SLM; Co-Cr-Mo alloy; Radially graded lattice structure; Compressive test; Microstructure; Fracture analysis

OPEN ACCESS

Citation: Cantaboni, F., Ginestra, P., Tocci, M, Avanzini, A., Ceretti, E., Pola, A. Compressive behavior of Co-Cr-Mo radially graded porous structures under as-built and heat-treated conditions, Frattura ed Integrità Strutturale, 62 (2020) 490-504.

Received: 11.08.2022
Accepted: 06.09.2022
Online first: 09.09.2022
Published: 01.10.2022

INTRODUCTION

AM technologies have an important impact on the biomedical industry due to the enhanced possibilities of customizations for the production of bespoke implants [1–6]. Of particular interest for the metallic materials are the powder bed fusion (PBF) processes, which can be split into categories based on the utilized energy source or the binding mechanism, e.g. selective laser sintering (SLS) and selective laser melting (SLM) [4,7–11].
Various alloys can be processed using Laser Powder Bed Fusion (L-PBF) processes, such as stainless steel, titanium, and cobalt alloys [12–14]. Among these, Co-Cr alloys have good versatility and durability, together with biocompatibility [15]. In general, these alloys are used to produce surgical tools and prostheses such as hip and knee replacements due to their excellent wear and corrosion resistance [16,17]. For this application, the stress-shielding effect can occur, since the prostheses should have a similar stiffness to the bone, otherwise osteoporosis issues can arise [18]. While this could be a limitation for metallic alloys with high elastic modulus, such as Co-Cr, with additive manufacturing, the use of cellular configurations can help to overcome this problem.
AM process can manufacture complex structures, taking advantage of layer-by-layer production. In comparison with other processing routes, it has more flexibility, together with the possibility to manufacture near-net-shape components without the need of expensive molds [19]. The lattice structures can be printed, that are topologically ordered and organized in 3D space with repeating open cells [20]. These structures are defined by node and strut dimensions (usually in the order of micrometres), and cell 3D dimensions. The stiffness of lattice structures can be tailored to be comparable with the physiological tissue while keeping the strength and biocompatibility of the Co-Cr alloys [21].
Lattice structures are composed of strut-based cell topologies, the most common are Body-Centered Cubic (BCC) and Face Centered Cubic (FCC) [22]. Moreover, other types of strut-based topologies exist, such as octet-truss, cubic, diagonal, and diamond [23]. Strut-based topologies can be characterized by the Maxwell number, M, which is calculated from the number of struts and nodes [24]. This number is useful to understand if the structures will be mechanically bending-dominated or stretch-dominated [25].
Besides cell geometry, the mechanical response of a lattice structure also depends on the material microstructure.
In this regard, an additional peculiar aspect of the L-PBF process is the extremely rapid solidification rate [15]. This influences the microstructure significantly, as already pointed out in the literature. In comparison with casting processes, the microstructure of Co-Cr alloy presents columnar grains growing in the building direction through the building layers, composed of fine cellular sub-grains [26].
Heat treatments may cause further modifications, providing the additional possibility to tune the lattice behavior according to the needs. In the literature [27], several heat treatments have been investigated to identify the effect of temperature, time, and cooling rate on the Co-Cr alloy samples manufactured by L-PBF. Heat treatments have a big influence on the mechanical properties, due to the microstructural changes they may induce [14,28].
In the present study, Face Centered Cubic (FCC), Diagonal (DG), and Diamond (DM) cells were selected and radially distributed for the lattice design due to their differences in terms of expected mechanical properties and porosity. The lattice structures were designed to investigate how the radial arrangement can affect the mechanical properties of the samples. This specific configuration is particularly relevant for biomedical applications, because the radially graded porosity is similar to the porosity of the physiological structure of the cortical bone, especially at the interface with trabecular bone lamellae [29–32]. Moreover, biocompatible radially graded porous structures have already been demonstrated to promote and guide the repair of bone defects [33]. However, a few studies are available in the literature regarding the mechanical characterization of these structures produced using Co-Cr alloy [18].
This work aims to analyse and report the mechanical characterization of innovative Co-Cr-Mo radially graded porous samples manufactured by L-PBF. Furthermore, the lattice structures were built with different orientations (i.e., horizontal and vertical) as a promising design strategy for biomedical applications involving tissue repair guidance and porosity control.

MATERIALS AND METHODS

Sample production and post-processing

Lattice structures were designed by 3D XPert software, (ProX® DMP 100, 3D system, Rock Hill, South Carolina, USA). Six cylindrical lattice samples with a height of 30 mm and a diameter of 24 mm with a nominal volume (Vn) of 13565 mm^3, were designed. The porosity was to be 50% or more, according to ISO 13314 standard, with three different unit cell geometry: Face Centered Cubic (FCC), Diamond (DM), and Diagonal (DG). The samples were produced with an orientation of 0° and 90° on the building plate (XY), as reported in Fig. 1a. Moreover, Fig. 1b shows the radial

gradient directions of the cells in relation to the Z-axis. A lower density than the uniformly distributed lattice structures was expected.
The volume of the cellular unit was 2(X) x 2(Y) x 2(Z) mm³. Nodal joints are designed with a spherical shape, with a diameter of 1.0 mm while the cross-sections of lattice struts are designed circular in shape with a diameter of 0,5 mm. The software can automatically generate the correct number of cells based on the dimension and the volume boundaries where it will be generated, setting the radial gradient as shown in Fig. 2.

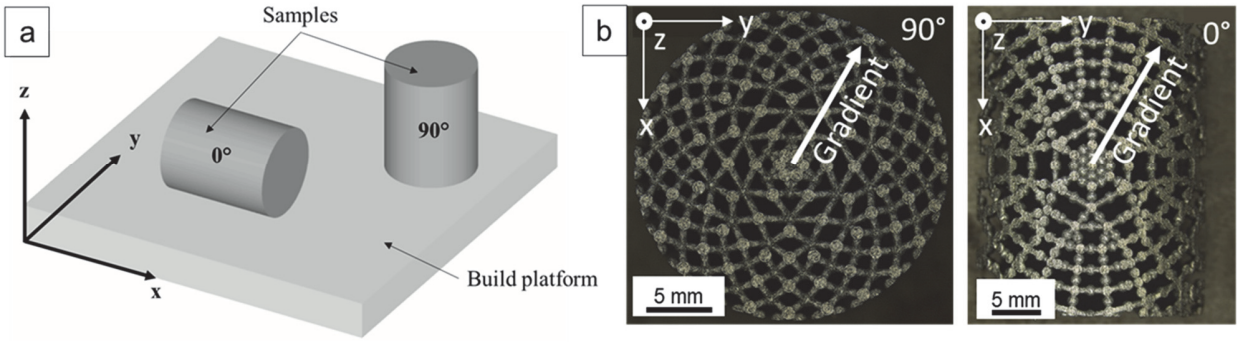

Figure 1: a) Orientations of the building samples on the building plate and b) the radial gradient direction of the cells.

The 90° and 0° radially graded porous lattices are reported in Fig. 2a, 3c, 3e and Fig. 2b, 3d, 3f, respectively. Therefore, the increasing gradient of porosity from the centre to the edges of samples can be tailored based on the orientation, as shown in Fig. 2. The samples are named respectively FCC0, FCC90, DM0, DM90, DG0, and DG90 due to their orientation in relation to the building plate.

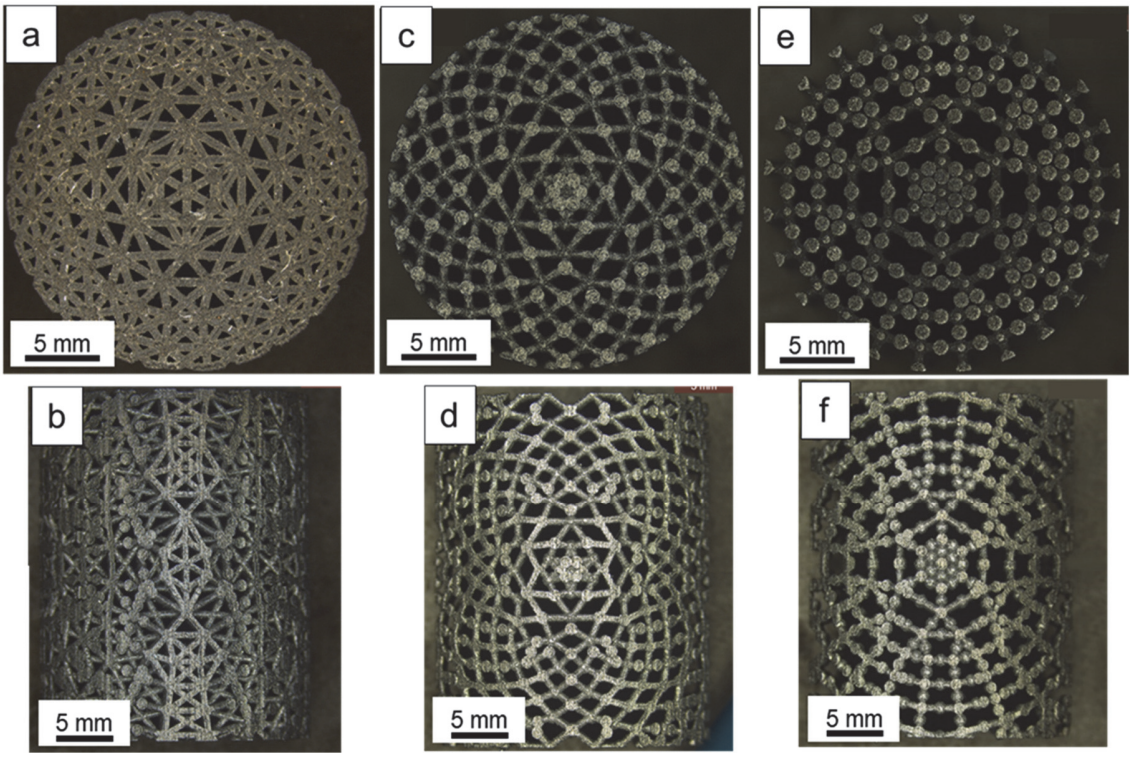

Figure 2: Radially graded porous lattice structures. Top view of: (a) FCC90, (c) DM90, (e) DG90 samples and side view of: (b) FCC0 (d) DM0, (f) DG0 samples.

Samples were manufactured using Co-Cr-Mo alloy powder produced by LaserForm®. The nominal chemical composition is reported in Table 1.

Co-Cr-Mo	Co	Cr	Mo	Ni	Fe	C	Si	Mn
Wt min (%)	Bal.	28.00	5.00	0.00	0.00	0.00	0.00	0.00
Wt max (%)		30.00	6.00	0.10	0.50	0.02	1.00	1.00

Table 1: Nominal chemical composition (wt%) of Co-Cr-Mo powders used for the production of samples.

The ProX® DMP 100 printer (3D system®, Wilsonville, Oregon, USA), was used for printing the lattices in a controlled nitrogen inert gas atmosphere (O2<0.01%) The printer process parameters were set as reported in Table 2:

Process Parameter	Value
Laser power [W]	50
Spot diameter [μm]	80
Scan speed [mm/s]	300
Hatch spacing [μm]	50
Layer thickness [μm]	30

Table 2: Process parameters used for the production of samples.

Supports were generated with the same process parameters as the lattice samples.
Where present, the supports for 90° samples were removed using a metallographic cutting machine. Then, the samples were grinded with sandpaper paying attention not to alter the lattice structure to assure the reliability of the mechanical tests.
Samples before and after heat treatment are named respectively as-built (AB) and heat-treated (HT) samples.
Heat treatment was performed using a horizontal furnace for vacuum heat treatment. The samples were heated from room temperature up to 1200 °C with a heating rate of 13°C/min and soaked at 1200°C for 2h. A partial pressure was applied as the temperature reached 650°C and upwards, while vacuum cooling was carried out. The aim was to relieve residual stresses and homogenize the microstructure [14].

Metallurgical, technological, and mechanical characterizations

The sample dimensions were collected to compare the designed model and produced samples. The diameter and height of the cylinders were experimentally measured with a Vernier caliper. The relative density was evaluated as the ratio between the total volume occupied by the material in relation to the geometry of the cell, based on the CAD file, and the total volume of the whole full cylinder [27].
The optical microscope (LEICA DMI 5000 M, Wetzlar, Germany) was used to investigate the microstructure of the samples. The as-built and heat-treated samples were mounted in acrylic resin, polished up to mirror finishing, and electrolytically etched (for 60 seconds in 5% HCl solution) to identify the main microstructural features. The software ImageJ (National Institutes of Health, USA) was used to measure the size of melting pools and laser scan tracks.
Moreover, Vickers microhardness measurements were performed with a Mitutoyo HM-200 (Mitutoyo Corporation, Kawasaki (Kanagawa), Japan) hardness testing machine to evaluate the effectiveness of the heat treatment. A load of 0.5 kg was applied for 15 s. Ten repetitions for each AB and HT sample were performed on the supports.
Compressions tests were carried out with a servo-hydraulic testing machine INSTRON 8501 (Instron, Norwood, MA, USA) equipped with a 500 kN load cell. Tests were conducted in displacement control at a constant crosshead velocity of 2 mm/min and the displacement was measured using the crosshead movement.
Load-displacement curves were generated from Instron output data. Maximum compressive strength (ultimate strength), quasi-elastic gradient, plateau stress between 20% to 40% strain, and compressive offset stress at the plastic compressive strain of 0.2 % (yield stress), were calculated according to ISO 13314:2011 standard. Ultimate strength was detected as the maximum stress, the quasi-elastic gradient was calculated considering the linear trend of the elastic field, and the yield stress was calculated with a 0.2% deviation of the quasi-elastic trend line. Plateau stress was calculated for bending-dominated samples as the average value of stress corresponding to the compressive strain from 20% to 40%, according to ISO 13314:2011. This is because their plateau was extended at higher values of strain, in contrast with stretch-dominated samples,

which present lower values of strain. The plateau stress was necessary to understand the behavior of the material and whether the response of the lattice was bending-dominated or stretch-dominated.
Furthermore, fracture surfaces of samples were analyzed by scanning electron microscope (SEM), LEO EVO® 40 (Carl Zeiss AG, Italy), to investigate the fracture mechanism.

RESULTS AND DISCUSSION

Lattice structure

A diameter of 24.1±0.1 mm was measured for the samples. Instead, a height of 30.3±0.1 mm was detected for the 0° samples in contrast with the 90° ones which resulted in a height of 28.6±0.5 mm, due to the support removal of the samples.
Moreover, the relative density was evaluated as a relevant parameter to determine the mechanical properties [1]. In Table 3 the relative density of the samples is reported, where VL is the volume of the designed samples and Vn (nominal volume) is 13565 mm3. The density changes with the kind of cells. The FCC configuration exhibits the highest density, due to the higher number of struts in its configuration.

Sample	Building angle [°]	VL [mm³]	Relative density [%]
FCC	0	6040	45
	90	5480	40
DM	0	3100	23
	90	3160	23
DG	0	2690	20
	90	2890	21

Table 3: Relative density of AB samples.

It is worth mentioning that partially melted powder may be trapped inside the samples due to their complex geometry, at the expense of mechanical behavior and relative density estimation [19,34].

Microstructure

Micrographs of the longitudinal (L) and transverse (T) cross-section of the 90° samples are shown in Fig. 3a and Fig. 3b. The microstructure of the 0° samples is not reported since they are characterized by the same features. The typical overlapped melt pools are shown in Fig. 3a on the L cross-section. They are caused by the melting powders under the focused laser energy. Instead, along the T cross-section, the elongated scan tracks are visible, revealing the pattern followed by the laser during the manufacturing process (Fig. 3b).
The dimension of melt pools was estimated along the L-section as reported in the literature [35]. The melt pools are semi-circular in shape and their dimension was compared with the laser beam diameter and layer thickness. The width and depth of melt pools range from 60 to 70 μm and from 30 to 35 μm, respectively. The average width is lower than the laser beam diameter, instead, the average depth is comparable with the layer thickness. This is due to the low value of laser power of 50W because it has been demonstrated that this parameter plays an important role in determining the size and geometry of melt pools, i.e. higher laser power leads to deeper melt pools [36,37].
Porosity defects typical of L-PBF components, such as spherical porosities due to trapped gas [38] or lack-of-fusion porosities, are also visible in Fig. 3a, and Fig. 3b.
In Fig. 3c and Fig. 3d, an extremely fine cellular sub-structure limited by melt pools boundary inside certain melt pools is visible. This metastable cellular microstructure is a peculiarity of the L-PBF technology, due to the extremely rapid solidification [39], and it is common for various alloys [40]. Unlike most metallic materials, for Co-Cr-Mo alloys, the cell boundaries can be distinguished due to the segregation of Mo and Cr, which surrounds the Co-Cr matrix, and not due to the presence of secondary phases, as recently reported in [40]. The cells are oriented in different directions inside the same

melt pool, as highlighted from the arrows in Fig. 3d, individuating different sub-grains that grow from the grain boundary following a preferential crystallographic orientation for Co-Cr alloy [39,40]. Since the grain growth is competitive, when they collide, one of them stops [41].
In addition, the micrographs reported in Fig. 3c and Fig. 3d show also examples of sintered particles and spatter, typical defects of components produced by L-PBF, usually characterized by poor surface finish in as-built conditions. In particular, the particle presented in Fig. 3d is characterized by a dendritic structure, indicating a solidification condition very different from the bulk material.

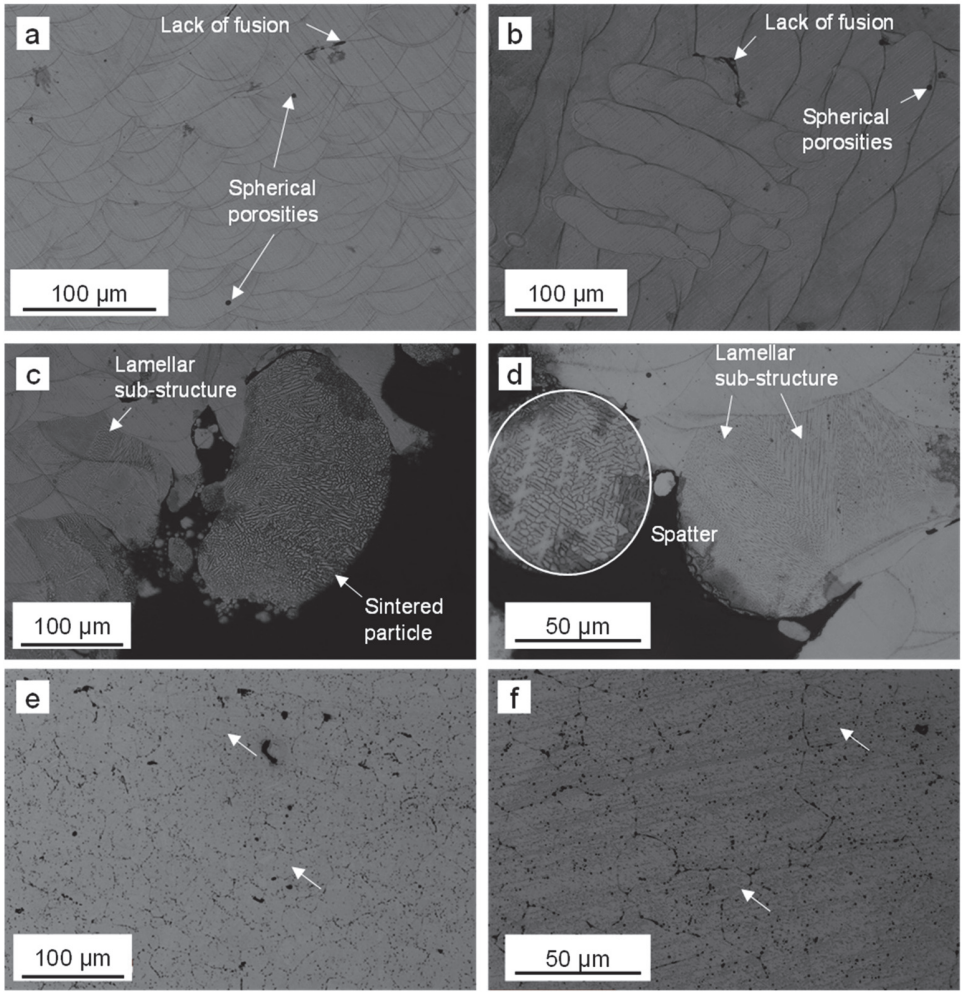

Figure 3: Optical micrographs of longitudinal (a) and transverse (b) cross-sections of AB samples built at 90°. Examples of sintered particles, cellular sub-structure (c), spatter, and lamellar sub-structure (d). Optical micrograph of HT sample (e) and HT sample at higher magnification (f) built at 90° (some examples of equiaxed grains marked by white arrows).

Regarding the grain structure, it is also well reported in the literature [32,42] that epitaxial columnar grains grow along the highest temperature gradient [43].
In contrast with AB samples, HT samples show a completely different microstructure, as reported in Fig. 3e. It clearly shows the disappearance of melt pools and the presence of equiaxed grains highlighted by the presence of precipitates along the grain boundaries. These are also dispersed in the matrix, as visible in Fig. 3f at higher magnification.
Various phenomena take place during heat treatment. During soaking at 1200 °C, the fine cellular structure is progressively fragmented and dissolved, leading to a more homogeneous distribution of solute atoms and the formation of precipitates [44]. The chemical composition of these particles is still a topic of discussion and further investigations are needed. A strong dependence on the chemical composition of the alloy is evident from the literature [40] and carbide particles [45] or Cr- and Mo-rich particles are identified according to the C level in the considered alloy [40]. In the present study, the extremely low content of C (0.02 wt. %) suggests that precipitates are mainly particles containing Cr and Mo rather than carbides. This is

consistent with a recent study [40] where a deep investigation of the evolution of microstructure during heat treatment is carried out.
Recrystallization also occurs, promoted by the high density of dislocations and residual stresses present in AB conditions, and resulting in coarse equiaxed grains after heat treatment (Fig. 3e and 3f). This is also discussed by [40,46–48].

Micro hardness

The hardness of AB samples built at 0° is 431 ± 9 HV and at 90° is 423 ± 11 HV, which is 24% and 29% higher compared to the hardness of the treated ones, 321 ± 10 HV and 318 ± 8 HV, respectively. A decrease of hardness in HT samples was observed. This is due to the microstructural change already discussed. In particular, the dissolution of the cellular structure and the recrystallization are mainly responsible for different strengthening mechanisms acting in the HT samples as compared to the AB ones, leading to the observed lower hardness. The effect of the building direction is negligible in HT ones. These results are supported by the literature [44,47–49].

Compressive properties of radially graded lattice structures

The stress-strain curves recorded during compression tests are shown in Fig. 4 where the corresponding cell morphology is indicated. The different behavior of the samples is noticeable in the different shapes of the curves reported in Fig. 4.
The test was considered completed when the samples started to collapse after bending to the ultimate strength value. From the graphs it is also possible to identify which samples are bending-dominated or stretch-dominated, following the Gibson Ashby law [20], considering that in stretch-dominated behavior the stress value is higher at a lower strain value.

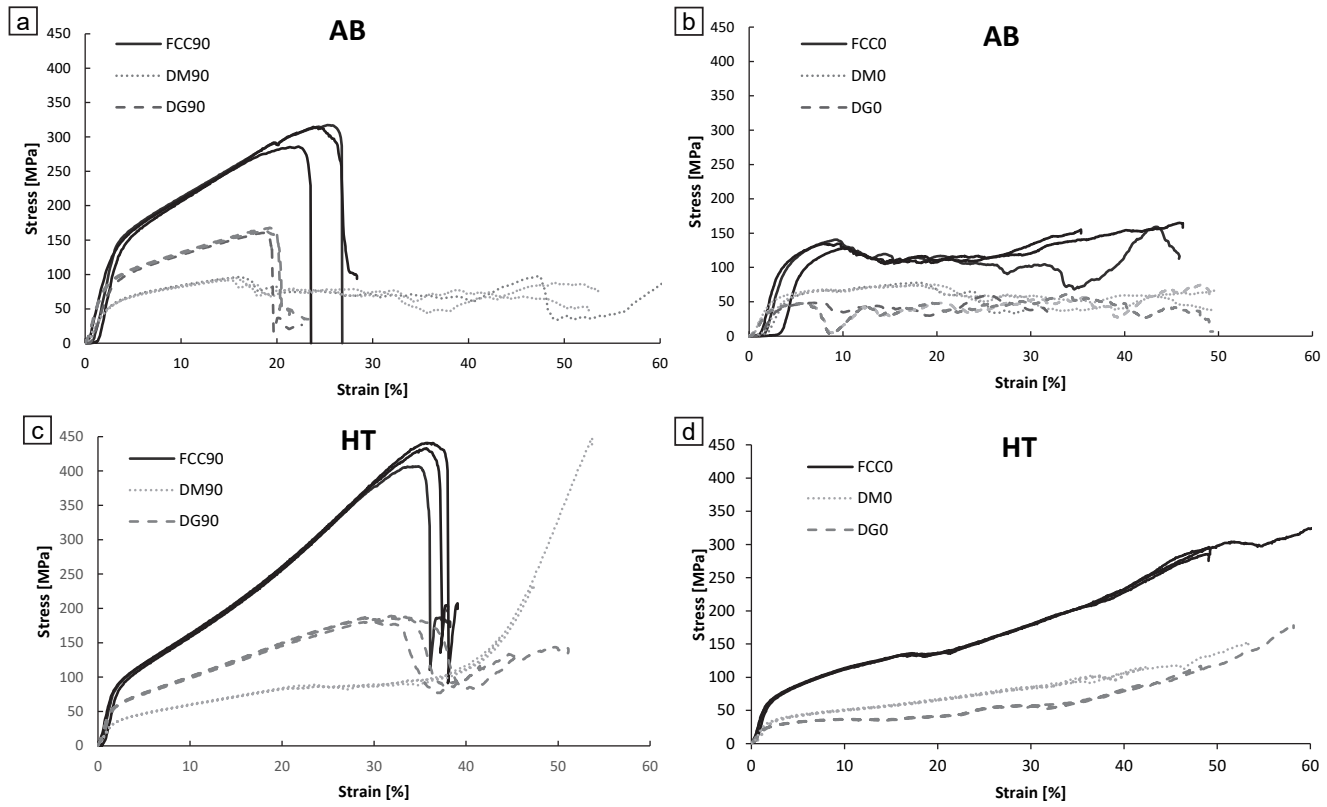

Figure 4: Stress-strain curves of: AB samples with: (a) FCC90, DM90, DG90 and (b) FCC0, DM0, DG0 (3 repetitions for each ones). HT samples with: (c) FCC90, DM90, DG90 and (d) FCC0, DM0, DG0 (3 repetitions for each ones).

For the 90° samples, the curves in Fig. 4a suggest that FCC90 and DG90 unit cells exhibit stretch-dominated behavior. In particular, the samples crashed at 306 ± 17 MPa at 25% of strain for FCC90 cells and 164 ± 4 MPa at 20% strain for DG90 cells. The curves of DM90 samples are instead characterized by bending-dominated behavior since they exhibit a more uniform trend, lower stress values, and deform more easily. The DM90 ultimate strength is 95 ± 3 MPa at 17% strain, followed by a decrease due to the collapse of the structure. Since strength is correlated with density, a higher value was expected for the DM cells samples in comparison with DG samples, due to the slightly lower relative density of unit DG

cells than the samples with DM cells [50]. The observed behavior could be caused by the radial orientation of cells as mentioned before. As expected, the samples with FCC cells, which featured the highest relative density, also exhibited the highest strength. In fact, for FCC AB samples the ultimate strength is 57% higher than for the DM and DG samples.
The stress-strain in Fig. 4b shows that DG0 unit cells exhibit stretch-dominated behavior which is crashed at 65 ± 9 MPa at 35% strain, while bending-dominated is typical for DM0 and FCC0 cells arrangement. These lasts crashed at 76 ± 2 MPa at 42% strain and 160 ± 5MPa at 18% strain, respectively.
Considering the influence of building orientation, for the AB specimens characterized by a stretch-dominated behavior, the resistance to compressive load is higher in the specimens built at 90° and on the contrary, the samples built at 0° can reach higher deformation. In fact, in Fig. 4b, it is possible to see that the 0° samples show a continuous increase in strain over 30% whereas, for the 90° ones (Fig. 4a), the strain at failure is in the order of 25%. These differences depend on the relation between struts orientation and load direction, the lattice configuration with higher strength and lower elongation at failure are those in which the unit cell has more struts oriented along the load direction.
For the samples characterized by bending-dominated behavior, represented by DM cell configuration, the effects mentioned above for the stretch-dominated behavior, are less marked, because neither in 0° samples nor in 90° ones the cells are oriented along the load direction.
Furthermore, the HT samples were investigated to confirm the AB results. They have a different mechanical response as shown in Fig. 4c and Fig. 4d. In general, they reach higher deformations than the AB samples. As shown in Fig. 4c, FCC90 samples collapsed at 427 ± 18 MPa at 35% strain and DG90 specimens at 185 ± 4 MPa at 30% strain, while the deformation of DM samples continued to increase over 40% strain, and they did not present a collapse point. FCC heat-treated samples showed an ultimate stress value 58% higher than DM and DG samples, due to the density of the structure geometries.
The DM and FCC samples built at 0° are the only ones having a bending-dominated behaviour and therefore a plateau-stress is reached. The plateau stress values of DM samples built at 0° and 90° were 75 MPa and 59 MPa, respectively, while for the FCC sample built at 0° was 112 MPa. In contrast with AB samples, the HT specimens do not present any plateau zone, because all of them are characterized by stretch-dominated behaviour, probably due to the transformation of the microstructure, which gives lower resistance, but higher isotropy and ductility.
Additionally, in Fig. 5a and Fig. 5b, a summary of results of quasi-elastic gradient and yield stress is reported.
The quasi-elastic gradient reported in Fig. 5a clearly shows that the influence of the building angle is almost negligible for FCC and DM structures. Regarding the DG samples, the values display a more pronounced deviation. Probably due to the building angle and the strut's distribution influence their stiffness. The DG samples exhibit different properties built at 0° and 90°.

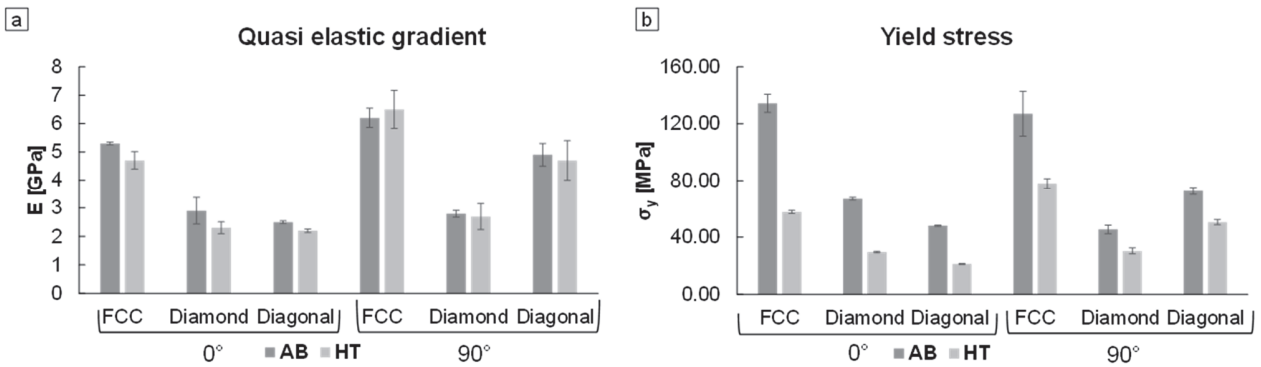

Figure 5: Average values with a standard deviation of quasi-elastic gradient (a) and yield stress (b) of the AB and HT samples.

The stiffness of AB and HT samples are similar, and their values differ by a maximum of 20%.
As shown in Fig. 5b, the build angle does not significantly affect the yield stress, as indicated for the quasi-elastic gradient analysis. The exception is still for the DG samples. Moreover, the heat treatment is extremely relevant, because the yield stress values remarkably decrease after the treatment, as shown in Fig. 5b. When the samples are heat-treated, the linear elastic zone is less wide compared with the AB samples. This is probably due to the homogenization and coarsening of the microstructure during heat treatment.
Both stiffness and strength data show an increase in accordance with the density, as expected.

The energy absorption data are reported in Fig. 6. After the heat treatment, it growths for all the samples independently from the cell morphology. This means that that the samples are able to reach higher deformation and therefore to absorb more energy when stressed.
This behavior is consistent with the decrease in hardness recorded after heat treatment and appears interesting for applications in the biomedical fields, such as for surgical implants and tools [2,50].

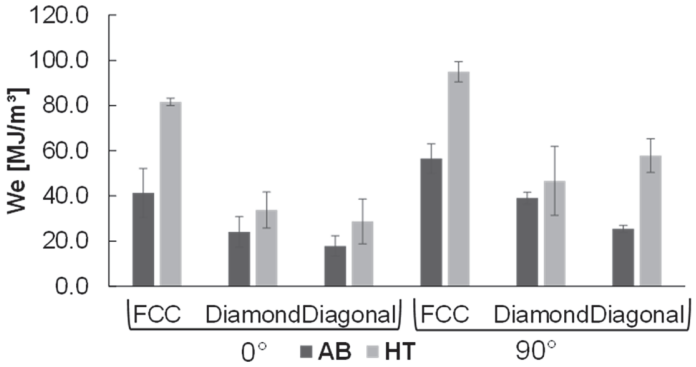

Figure 6: Energy absorption values of the samples.

The reported mechanical performance is in accordance with the literature [18,32,49,51-53]. In particular, the results obtained were compared with the literature to identify the main differences between the radially graded porous structure and uniformly distributed ones. The mechanical properties such as ultimate strength, yield stress, hardness, and energy absorption presented similar values for each configuration of the cell [1], [32], [37,53–55]. Instead, the radial arrangements give the lattices a stiffness homogenization along the planes perpendicular to the symmetry axis, contrary to the non-radially graded lattices, which are characterized by anisotropic stiffness [56,57].

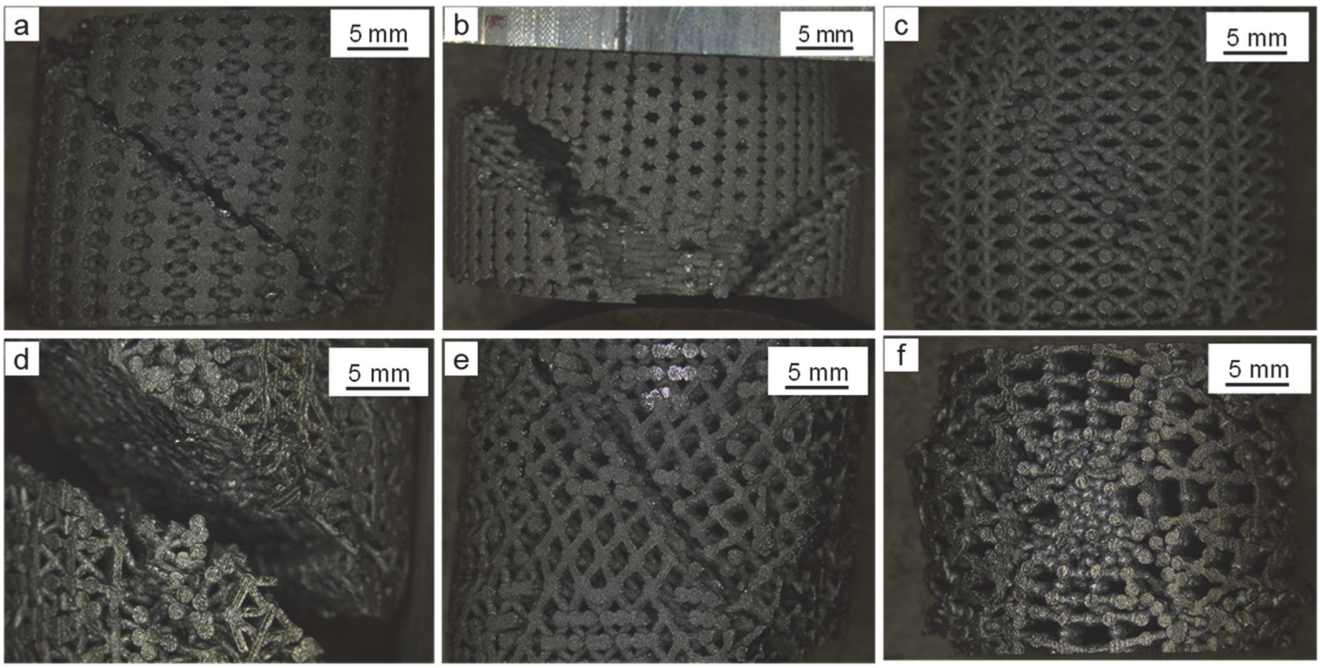

Figure 7: Main failure modes after compression test on AB sample: a) FCC90, b) DM90, c) DG90, d) FCC0, e) DM0 and f) DG0.

Failure modes and Fracture analysis

The compression tests were ended after the first major structural collapse, usually signified by the fracture of the specimen into multiple pieces. Otherwise, they were terminated when the sample reached the strain of 50%-60%.
Some examples of specimen failure, representative of the analysed AB samples, are reported in Figure 7.

Most of the specimens showed the presence of an inclined plane along which final failure occurred, although with some differences. For FCC90 and DG90 (Fig. 7a and Fig. 7c) failure was almost simultaneous along with layers at different heights and, as shown in Fig. 5a, no plateau was observed. For DM90, FCC0 and DM0 (Fig. 7b, Fig. 7d, and Fig. 7e) failure were more progressive and a plateau with small fluctuation was present (see Fig. 4a and Fig. 4b). On the contrary, DG0 samples (Fig. 7f) progressively crashed layer after layer and the plateau showed more evident fluctuations (Fig. 4b), suggesting a brittle nature of the failure mechanism.
Some examples of heat-treated specimen failure, representative of all the analysed ones is reported in Fig. 8, again with the presence of different failure modes. In particular, while the FCC90 and the DG90 (Fig. 8a and Fig. 8c) failed similarly to the AB condition and the stress-strain behavior is of the same type (Fig. 4c), the DM90 (Fig. 8b) progressively crushed with a more extended and flatter plateau and very limited stress fluctuations.
A similar response was observed (Fig. 4d) for FCC0 (Fig. 8d), with some discontinuities related to sudden local failures, and for DM0 and DG0 (Fig. 8e and Fig. 8f). For this latter condition, by comparison with AB, a damping effect due to the increased ductility related to HT can be appreciated.

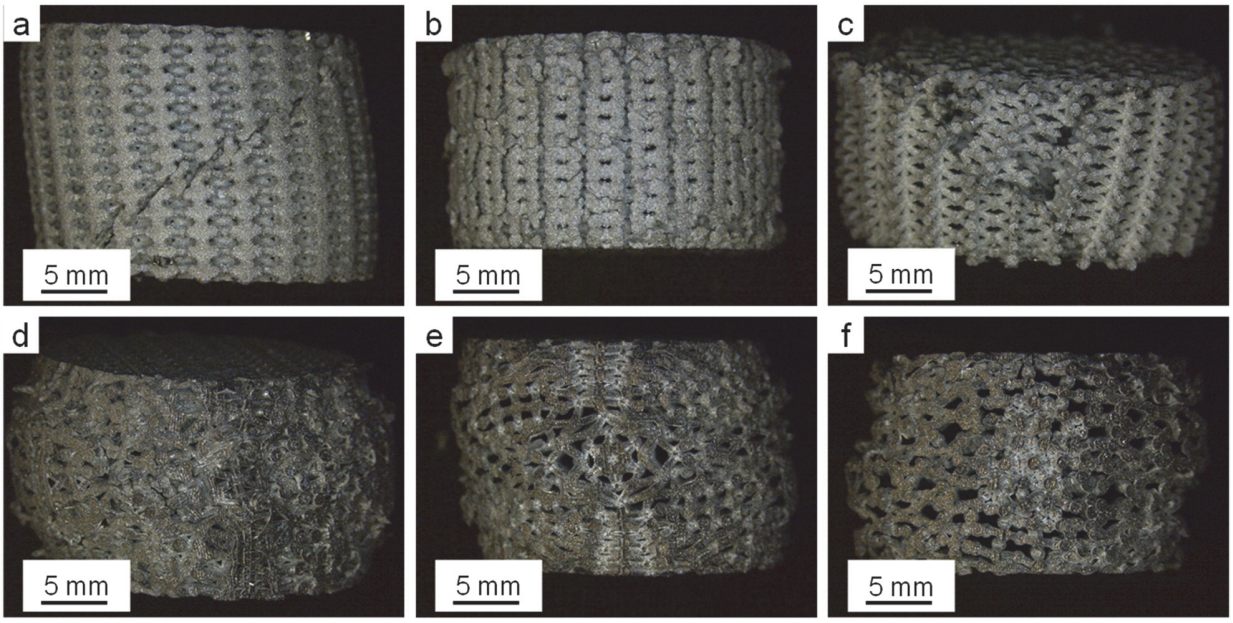

Figure 8: Main failure modes after compression test on HT samples: (a) FCC90, (b) DM90, c) DG90, d) FCC0, e) DM0 and f) DG0.

Overall, the different failure modes observed at the macroscopical level agree with the literature confirming that by exploiting different combinations of lattice cell configurations, orientation, and post-treatments a variety of deformation behaviors can be achieved. The change of the failure mode through the heat treatment can be shown in other metals [22,58,59].
Representative SEM images of the fracture surface of the AB samples are shown in Fig. 9a, Fig. 9b, and Fig. 9c. Images related only to FCC and DG samples are shown since no different role of the microstructure was identified changing the design of the geometry of the lattice.
At low magnification (Fig. 9a), details indicating a quasi-cleavage mechanism can be observed, as flat areas with parallel markings. Terrace-like steps were also presents where the fracture is crossing grain boundaries, probably due to the presence of defects that guide the fracture propagation. Similar features in terms of fracture behavior were also found in the literature [43,44] for samples after tensile tests, such as terrace-like steps and cleavage facets.
Additional features can be identified by observing the specimen at higher magnification (Fig. 9b, Fig. 9c). For instance, the elongated markings indicated by arrows in Fig. 9b resemble the elongated cellular structure visible in the melt pools suggesting that these can influence the direction of fracture propagation. Similarly, according to the fracture propagation, the cell structure can be crossed in a normal direction. In this case, instead of elongated markings, a dimple-like structure may be detected, as in Fig. 9c. The size of these dimples is comparable with the cell spacing of the samples (Fig. 3) and this is also confirmed by the literature [46,58].

In contrast, larger areas that exhibit ductile fracture are visible in HT sample [60], as shown in Fig. 9d. Coarser dimples than in AB samples are present probably due to the loss of extra-fine microstructure after heat treatment (Fig. 9e). Moreover, the presence of fine particles at the center of the dimples is shown in Fig. 9f. These fine particles are detected only in the HT samples, and they are associated with the formation of coarse precipitates during heat treatment, as visible in Fig. 3e.

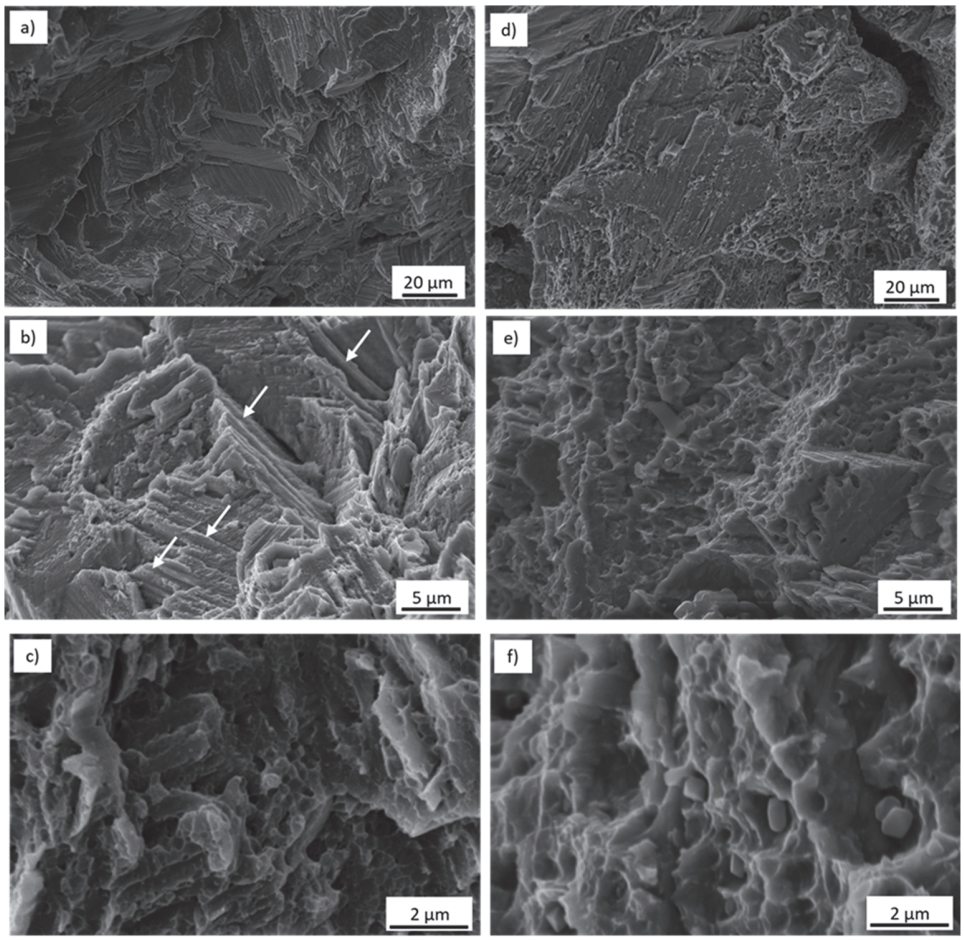

Figure 8: Representative SEM images of fracture mechanism of AB samples (a), (b), (c), and HT samples (d), (e), (f).

Conclusions

The main aim of this work was to analyse the compression behavior of Co-Cr-Mo radially graded lattice structure, manufactured by L-PBF aimed to biomedical applications. Different lattice configurations printed at 0° and 90° build angles were considered to investigate the variation in sample properties due to the different orientations of the struts of FCC, DM and DG cells with a radial gradient direction. Moreover, the samples were heat-treated to study the consequent evolution of the mechanical properties.

Based on the experimental results and discussion, it can be concluded that:

- The building orientation resulted an important parameter affecting the mechanical response of the structures. In fact, for the AB samples, the ultimate stress of 90° samples is higher than for the 0° ones. In particular, the ultimate stress of FCC, DM, and DG samples built at 90° is 48%, 20%, and 61% higher than for those built at 0°, respectively. Both stiffness and strength showed a growing trend with the increase in density, where FCC showed the highest value.
- For all three geometries, the radially graded porous structures exhibited different mechanical properties according to the orientation at 0° or 90° of the samples. The 0° specimens showed a continuous increase in strain over 30% while, for the 90° ones, at 25% strain the structure collapsed. These differences depend on the relationship between

struts orientation and load direction. In particular, the lattice configuration with higher strength and lower elongation at failure are those in which the unit cell has more struts oriented along the load direction.

- In general, the HT samples exhibited a more ductile behavior since a decrease in stiffness and hardness of the samples was recorded. This is consistent with the mainly ductile fracture behavior detected from the analysis of fracture surfaces, while AB structures exhibited features of a quasi-cleavage mechanism.

The possibility to produce radially graded lattice structures was demonstrated. Moreover, it was shown how the mechanical properties are affected by cell geometry and orientation in combination with heat treatment. The obtained results give further insight into the possibility to tailor the mechanical properties of lattice structures according to a specific selected application. Therefore, the achieved results can open novel solutions for the proper repair of local defects within the bone and the acceleration of the regeneration of the physiological tissue due to the combination of mechanical and morphological stimuli. Additionally, the proposed configurations could represent an optimal solution to produce customized metal implants.

ACKNOWLEDGMENT

The authors deeply thank Mr. L. Lauri for support in SEM analysis and Mr. L. Riva for the production of samples.

REFERENCES

[1] Riva, L., Ginestra, P.S., Ceretti, E. (2021). Mechanical characterization and properties of laser-based powder bed–fused lattice structures: a review, Int. J. Adv. Manuf. Technol., 113(3–4), pp. 649–671, DOI: 10.1007/s00170-021-06631-4.

[2] Buj-Corral, I., Tejo-Otero, A., Fenollosa-Artés, F. (2020). Development of am technologies for metals in the sector of medical implants, Metals (Basel)., 10(5), pp. 1–30, DOI: 10.3390/met10050686.

[3] Johnson, N.S., Vulimiri, P.S., To, A.C., Zhang, X., Brice, C.A., Kappes, B.B., Stebner, A.P. (2020). Invited review: Machine learning for materials developments in metals additive manufacturing, Addit. Manuf., 36, DOI: 10.1016/j.addma.2020.101641.

[4] Wang, C., Tan, X.P., Tor, S.B., Lim, C.S. (2020). Machine learning in additive manufacturing: State-of-the-art and perspectives, Addit. Manuf., 36(August), pp. 101538, DOI: 10.1016/j.addma.2020.101538.

[5] Ginestra, P., Ferraro, R.M., Zohar-Hauber, K., Abeni, A., Giliani, S., Ceretti, E. (2020). Selective laser melting and electron beam melting of Ti6Al4V for orthopedic applications: A comparative study on the applied building direction, Materials (Basel)., 13(23), pp. 1–23, DOI: 10.3390/ma13235584.

[6] Ginestra, P., Ceretti, E., Lobo, D., Lowther, M., Cruchley, S., Kuehne, S., Villapun, V., Cox, S., Grover, L., Shepherd, D., Attallah, M., Addison, O., Webber, M. (2020). Post processing of 3D printed metal scaffolds: A preliminary study of antimicrobial efficiency, Procedia Manuf., 47(2019), pp. 1106–1112, DOI: 10.1016/j.promfg.2020.04.126.

[7] Sing, S.L., An, J., Yeong, W.Y., Wiria, F.E. (2016). Laser and electron-beam powder-bed additive manufacturing of metallic implants: A review on processes, materials and designs, J. Orthop. Res., 34(3), pp. 369–385, DOI: 10.1002/jor.23075.

[8] Gu, D.D., Meiners, W., Wissenbach, K., Poprawe, R. (2012). Laser additive manufacturing of metallic components: Materials, processes and mechanisms, Int. Mater. Rev., 57(3), pp. 133–164, DOI: 10.1179/1743280411Y.0000000014.

[9] Murr, L.E., Quinones, S.A., Gaytan, S.M., Lopez, M.I., Rodela, A., Martinez, E.Y., Hernandez, D.H., Martinez, E., Medina, F., Wicker, R.B. (2009). Microstructure and mechanical behavior of Ti-6Al-4V produced by rapid-layer manufacturing, for biomedical applications, J. Mech. Behav. Biomed. Mater., 2(1), pp. 20–32, DOI: 10.1016/j.jmbbm.2008.05.004.

[10] Murr, L.E., Esquivel, E. V., Quinones, S.A., Gaytan, S.M., Lopez, M.I., Martinez, E.Y., Medina, F., Hernandez, D.H., Martinez, E., Martinez, J.L., Stafford, S.W., Brown, D.K., Hoppe, T., Meyers, W., Lindhe, U., Wicker, R.B. (2009). Microstructures and mechanical properties of electron beam-rapid manufactured Ti-6Al-4V biomedical prototypes compared to wrought Ti-6Al-4V, Mater. Charact., 60(2), pp. 96–105, DOI: 10.1016/j.matchar.2008.07.006.

[11] Mazzoli, A. (2013). Selective laser sintering in biomedical engineering, Med. Biol. Eng. Comput., 51(3), pp. 245–256, DOI: 10.1007/s11517-012-1001-x.

[12] Ginestra, P.S., Riva, L., Allegri, G., Giorleo, L., Attanasio, A., Ceretti, E. (2020). Analysis of 3D printed 17-4 PH stainless steel lattice structures with radially oriented cells, Ind. 4.0 – Shap. Futur. Digit. World, , pp. 136–141, DOI: 10.1201/9780367823085-25.
[13] Bayat, M., Thanki, A., Mohanty, S., Witvrouw, A., Yang, S., Thorborg, J., Tiedje, N.S., Hattel, J.H. (2019). Keyhole-induced porosities in Laser-based Powder Bed Fusion (L-PBF) of Ti6Al4V: High-fidelity modelling and experimental validation, Addit. Manuf., 30, pp. 100835, DOI: 10.1016/j.addma.2019.100835.
[14] Razavi, S.M.J., Avanzini, A., Cornacchia, G., Giorleo, L., Berto, F. (2021). Effect of heat treatment on fatigue behavior of as-built notched Co-Cr-Mo parts produced by Selective Laser Melting, Int. J. Fatigue, 142, pp. 105926, DOI: 10.1016/j.ijfatigue.2020.105926.
[15] Wang, J.H., Ren, J., Liu, W., Wu, X.Y., Gao, M.X., Bai, P.K. (2018). Effect of selective laser melting process parameters on microstructure and properties of Co-Cr alloy, Materials (Basel), 11(9), DOI: 10.3390/ma11091546.
[16] Gupta, S.K., Shahidsha, N., Bahl, S., Kedaria, D., Singamneni, S., Yarlagadda, P.K.D.V., Suwas, S., Chatterjee, K. (2021). Enhanced biomechanical performance of additively manufactured Ti-6Al-4V bone plates, J. Mech. Behav. Biomed. Mater., 119(March), pp. 104552, DOI: 10.1016/j.jmbbm.2021.104552.
[17] Henriques, B., Bagheri, A., Gasik, M., Souza, J.C.M., Carvalho, O., Silva, F.S., Nascimento, R.M. (2015). Mechanical properties of hot pressed CoCrMo alloy compacts for biomedical applications, Mater. Des., 83, pp. 829–834, DOI: 10.1016/j.matdes.2015.06.069.
[18] Limmahakhun, S., Oloyede, A., Sitthiseripratip, K., Xiao, Y., Yan, C. (2017). Stiffness and strength tailoring of cobalt chromium graded cellular structures for stress-shielding reduction, Mater. Des., 114, pp. 633–641, DOI: 10.1016/j.matdes.2016.11.090.
[19] Jin, N., Yan, Z., Wang, Y., Cheng, H., Zhang, H. (2021). Effects of heat treatment on microstructure and mechanical properties of selective laser melted Ti-6Al-4V lattice materials, Int. J. Mech. Sci., 190, pp. 106042, DOI: 10.1016/j.ijmecsci.2020.106042.
[20] Maconachie, T., Leary, M., Lozanovski, B., Zhang, X., Qian, M., Faruque, O., Brandt, M. (2019). SLM lattice structures: Properties, performance, applications and challenges, Mater. Des., 183, pp. 108137, DOI: 10.1016/j.matdes.2019.108137.
[21] Liverani, E., Rogati, G., Pagani, S., Brogini, S., Fortunato, A., Caravaggi, P. (2021). Mechanical interaction between additive-manufactured metal lattice structures and bone in compression: implications for stress shielding of orthopaedic implants, J. Mech. Behav. Biomed. Mater., 121(March), pp. 104608, DOI: 10.1016/j.jmbbm.2021.104608.
[22] Maskery, I., Aboulkhair, N.T., Aremu, A.O., Tuck, C.J., Ashcroft, I.A. (2017). Compressive failure modes and energy absorption in additively manufactured double gyroid lattices, Addit. Manuf., 16, pp. 24–29, DOI: 10.1016/j.addma.2017.04.003.
[23] Amin Yavari, S., Ahmadi, S.M., Wauthle, R., Pouran, B., Schrooten, J., Weinans, H., Zadpoor, A.A. (2015). Relationship between unit cell type and porosity and the fatigue behavior of selective laser melted meta-biomaterials, J. Mech. Behav. Biomed. Mater., 43, pp. 91–100, DOI: 10.1016/j.jmbbm.2014.12.015.
[24] Abdelhamid, M., Czekanski, A. (2018). Impact of the lattice angle on the effective properties of the octet-truss lattice structure, J. Eng. Mater. Technol. Trans. ASME, 140(4), pp. 1747–1769, DOI: 10.1115/1.4040409.
[25] Leary, M., Mazur, M., Williams, H., Yang, E., Alghamdi, A., Lozanovski, B., Zhang, X., Shidid, D., Farahbod-Sternahl, L., Witt, G., Kelbassa, I., Choong, P., Qian, M., Brandt, M. (2018). Inconel 625 lattice structures manufactured by selective laser melting (SLM): Mechanical properties, deformation and failure modes, Mater. Des., 157, pp. 179–199, DOI: 10.1016/j.matdes.2018.06.010.
[26] Anantharaj, S., Kundu, S., Noda, S. (2020). Ur n al Pr, Nano Energy, , pp. 105514, DOI: 10.1016/j.addma.2021.102025.
[27] Alomar, Z., Concli, F. (2020). A Review of the Selective Laser Melting Lattice Structures and Their Numerical Models, Adv. Eng. Mater., 22(12), pp. 1–17, DOI: 10.1002/adem.202000611.
[28] Guoqing, Z., Junxin, L., Xiaoyu, Z., Jin, L., Anmin, W. (2018). Effect of Heat Treatment on the Properties of CoCrMo Alloy Manufactured by Selective Laser Melting, J. Mater. Eng. Perform., 27(5), pp. 2281–2287, DOI: 10.1007/s11665-018-3351-5.
[29] Alabort, E., Barba, D., Reed, R.C. (2019). Design of metallic bone by additive manufacturing, Scr. Mater., 164, pp. 110–114, DOI: 10.1016/j.scriptamat.2019.01.022.
[30] Di Luca, A., Longoni, A., Criscenti, G., Mota, C., Van Blitterswijk, C., Moroni, L. (2016). Toward mimicking the bone structure: Design of novel hierarchical scaffolds with a tailored radial porosity gradient, Biofabrication, 8(4), DOI: 10.1088/1758-5090/8/4/045007.
[31] Barba, D., Alabort, E., Reed, R.C. (2019). Synthetic bone: Design by additive manufacturing, Acta Biomater., 97, pp. 637–656, DOI: 10.1016/j.actbio.2019.07.049.

[32] Caravaggi, P., Liverani, E., Leardini, A., Fortunato, A., Belvedere, C., Baruffaldi, F., Fini, M., Parrilli, A., Mattioli-Belmonte, M., Tomesani, L., Pagani, S. (2019). CoCr porous scaffolds manufactured via selective laser melting in orthopedics: Topographical, mechanical, and biological characterization, J. Biomed. Mater. Res. - Part B Appl. Biomater., 107(7), pp. 2343–2353, DOI: 10.1002/jbm.b.34328.

[33] Xie, J., MacEwan, M.R., Ray, W.Z., Liu, W., Siewe, D.Y., Xia, Y. (2010). Radially aligned, electrospun nanofibers as dural substitutes for wound closure and tissue regeneration applications, ACS Nano, 4(9), pp. 5027–5036, DOI: 10.1021/nn101554u.

[34] Mahmoudi, M., Elwany, A., Yadollahi, A., Thompson, S.M., Bian, L., Shamsaei, N. (2017). Mechanical properties and microstructural characterization of selective laser melted 17-4 PH stainless steel, Rapid Prototyp. J., 23(2), pp. 280–294, DOI: 10.1108/RPJ-12-2015-0192.

[35] Seede, R., Shoukr, D., Zhang, B., Whitt, A., Gibbons, S., Flater, P., Elwany, A., Arroyave, R., Karaman, I. (2020). An ultra-high strength martensitic steel fabricated using selective laser melting additive manufacturing: Densification, microstructure, and mechanical properties, Acta Mater., 186, pp. 199–214, DOI: 10.1016/j.actamat.2019.12.037.

[36] Zhao, C., Fezzaa, K., Cunningham, R.W., Wen, H., De Carlo, F., Chen, L., Rollett, A.D., Sun, T. (2017). Real-time monitoring of laser powder bed fusion process using high-speed X-ray imaging and diffraction, Sci. Rep., 7(1), pp. 1–11, DOI: 10.1038/s41598-017-03761-2.

[37] Darvish, K., Chen, Z.W., Phan, M.A.L., Pasang, T. (2018). Selective laser melting of Co-29Cr-6Mo alloy with laser power 180–360 W: Cellular growth, intercellular spacing and the related thermal condition, Mater. Charact., 135(September 2017), pp. 183–191, DOI: 10.1016/j.matchar.2017.11.042.

[38] Zhang, B., Li, Y., Bai, Q. (2017). Defect Formation Mechanisms in Selective Laser Melting: A Review, Chinese J. Mech. Eng. (English Ed., 30(3), pp. 515–527, DOI: 10.1007/s10033-017-0121-5.

[39] Prashanth, K.G., Eckert, J. (2017). Formation of metastable cellular microstructures in selective laser melted alloys, J. Alloys Compd., 707, pp. 27–34, DOI: 10.1016/j.jallcom.2016.12.209.

[40] Roudnická, M., Molnárová, O., Drahokoupil, J., Kubásek, J., Bigas, J., Šreibr, V., Paloušek, D., Vojtěch, D. (2021). Microstructural instability of L-PBF Co-28Cr-6Mo alloy at elevated temperatures, Addit. Manuf., 44(April), pp. 102025, DOI: 10.1016/j.addma.2021.102025.

[41] Chen, Z.W., Phan, M.A.L., Darvish, K. (2017). Grain growth during selective laser melting of a Co–Cr–Mo alloy, J. Mater. Sci., 52(12), pp. 7415–7427, DOI: 10.1007/s10853-017-0975-z.

[42] Takaichi, A., Suyalatu., Nakamoto, T., Joko, N., Nomura, N., Tsutsumi, Y., Migita, S., Doi, H., Kurosu, S., Chiba, A., Wakabayashi, N., Igarashi, Y., Hanawa, T. (2013). Microstructures and mechanical properties of Co-29Cr-6Mo alloy fabricated by selective laser melting process for dental applications, J. Mech. Behav. Biomed. Mater., 21, pp. 67–76, DOI: 10.1016/j.jmbbm.2013.01.021.

[43] Tonelli, L., Fortunato, A., Ceschini, L. (2020). CoCr alloy processed by Selective Laser Melting (SLM): effect of Laser Energy Density on microstructure, surface morphology, and hardness, J. Manuf. Process., 52, pp. 106–119, DOI: 10.1016/j.jmapro.2020.01.052.

[44] Zhang, M., Yang, Y., Song, C., Bai, Y., Xiao, Z. (2018). An investigation into the aging behavior of CoCrMo alloys fabricated by selective laser melting, J. Alloys Compd., 750, pp. 878–886, DOI: 10.1016/j.jallcom.2018.04.054.

[45] Sing, S.L., Huang, S., Yeong, W.Y. (2020). Effect of solution heat treatment on microstructure and mechanical properties of laser powder bed fusion produced Co-28Cr-6Mo, Mater. Sci. Eng. A, 769, pp. 138511, DOI: 10.1016/j.msea.2019.138511.

[46] Bawane, K.K., Srinivasan, D., Banerjee, D. (2018). Microstructural Evolution and Mechanical Properties of Direct Metal Laser-Sintered (DMLS) CoCrMo After Heat Treatment, Metall. Mater. Trans. A Phys. Metall. Mater. Sci., 49(9), pp. 3793–3811, DOI: 10.1007/s11661-018-4771-4.

[47] Kajima, Y., Takaichi, A., Kittikundecha, N., Nakamoto, T., Kimura, T., Nomura, N., Kawasaki, A., Hanawa, T., Takahashi, H., Wakabayashi, N. (2018). Effect of heat-treatment temperature on microstructures and mechanical properties of Co–Cr–Mo alloys fabricated by selective laser melting, Mater. Sci. Eng. A, 726, pp. 21–31, DOI: 10.1016/j.msea.2018.04.048.

[48] Tonelli, L., Boromei, I., Liverani, E., Ceschini, L. (2021). Microstructural evolution induced by heat treatment in the Co28Cr6Mo alloy produced by selective laser melting, Metall. Ital., 113(2), pp. 22–30.

[49] Dolgov, N, A., Dikova, T., Dzhendov, D., Pavlova, D., Simov, M. (2016). Mechanical Properties of Dental Co-Cr Alloys Fabricated via Casting and Selective Laser Melting, Sci. Proc. Ii Int. Sci. Conf. Innovations Eng. 2016, 33, pp. 29–33.

[50] Liu, F., Zhang, D.Z., Zhang, P., Zhao, M., Jafar, S. (2018). Mechanical properties of optimized diamond lattice structure for bone scaffolds fabricated via selective laser melting, Materials (Basel), 11(3), DOI: 10.3390/ma11030374.

[51] Özeren, E., Altan, M. (2020). Effect of structural hybrid design on mechanical and biological properties of CoCr scaffolds fabricated by selective laser melting, Rapid Prototyp. J., 26(4), pp. 615–624, DOI: 10.1108/RPJ-07-2019-0186.
[52] Van Hooreweder, B., Kruth, J.P. (2017). Advanced fatigue analysis of metal lattice structures produced by Selective Laser Melting, CIRP Ann. - Manuf. Technol., 66(1), pp. 221–224, DOI: 10.1016/j.cirp.2017.04.130.
[53] Cutolo, A., Neirinck, B., Lietaert, K., de Formanoir, C., Van Hooreweder, B. (2018). Influence of layer thickness and post-process treatments on the fatigue properties of CoCr scaffolds produced by laser powder bed fusion, Addit. Manuf., 23, pp. 498–504, DOI: 10.1016/j.addma.2018.07.008.
[54] Koizumi, Y., Okazaki, A., Chiba, A., Kato, T., Takezawa, A. (2016). Cellular lattices of biomedical Co-Cr-Mo-alloy fabricated by electron beam melting with the aid of shape optimization, Addit. Manuf., 12, pp. 305–313, DOI: 10.1016/j.addma.2016.06.001.
[55] Lu, Y., Wu, S., Gan, Y., Zhang, S., Guo, S., Lin, J., Lin, J. (2016). Microstructure, mechanical property and metal release of As-SLM CoCrW alloy under different solution treatment conditions, J. Mech. Behav. Biomed. Mater., 55, pp. 179–190, DOI: 10.1016/j.jmbbm.2015.10.019.
[56] Tan, X.P., Tan, Y.J., Chow, C.S.L., Tor, S.B., Yeong, W.Y. (2017). Metallic powder-bed based 3D printing of cellular scaffolds for orthopaedic implants: A state-of-the-art review on manufacturing, topological design, mechanical properties and biocompatibility, Mater. Sci. Eng. C, 76, pp. 1328–1343, DOI: 10.1016/j.msec.2017.02.094.
[57] Hacisalihoğlu, İ., Yildiz, F., Çelik, A. (2021). Experimental and Numerical Investigation of Mechanical Properties of Different Lattice Structures Manufactured from Medical Titanium Alloy by Using Laser Beam-Powder Bed Fusion, J. Mater. Eng. Perform., 30(7), pp. 5466–5476, DOI: 10.1007/s11665-021-05865-3.
[58] Obadimu, S.O., Kourousis, K.I. (2021). Compressive behaviour of additively manufactured lattice structures: A review, Aerospace, 8(8), DOI: 10.3390/aerospace8080207.
[59] Cutolo, A., Engelen, B., Desmet, W., Van Hooreweder, B. (2020). Mechanical properties of diamond lattice Ti–6Al–4V structures produced by laser powder bed fusion: On the effect of the load direction, J. Mech. Behav. Biomed. Mater., 104, DOI: 10.1016/j.jmbbm.2020.103656.
[60] Song, C., Zhang, M., Yang, Y., Wang, D., Jia-kuo, Y. (2018). Morphology and properties of CoCrMo parts fabricated by selective laser melting, Mater. Sci. Eng. A, 713, pp. 206–213, DOI: 10.1016/j.msea.2017.12.035.